The Astrophysical Journal, 1005:223 (12pp), 2026 July 10 https://doi.org/10.3847/1538-4357/ae77f2

An Updated Infrared Solar Spectrum from ACE-FTS and a CH Rovibrational Line List

Manish Bhusal[1], Peter F. Bernath[1,2,3], Léo Lavy[2], Chris D. Boone[3], and Frank Hase[4]
[1] Department of Physics, Old Dominion University, Norfolk, VA 23529, USA; mbhus001@odu.edu
[2] Department of Chemistry and Biochemistry, Old Dominion University, Norfolk, VA 23529, USA
[3] Department of Chemistry, University of Waterloo, Waterloo, ON, N2L 3G1, Canada
[4] Karlsruhe Institute of Technology (KIT), Institute of Meteorology and Climate Research (IMKASF), Karlsruhe, Germany
Received 2026 March 12; revised 2026 May 18; accepted 2026 May 21; published 2026 July 8

Abstract

An updated Atmospheric Chemistry Experiment Fourier Transform Spectrometer infrared solar spectrum has been produced from low-Earth orbit covering 1829–4440 cm^{-1} (2.252–5.467 μm). Spectroscopic constants for the $v = 4$ and $v = 5$ vibrational levels of the $X^2\Pi$ state of CH radical have been updated by incorporating additional vibration–rotation lines from the new solar spectrum and from an archival laboratory spectrum. New ab initio calculations of the permanent dipole moment function for the $X^2\Pi$ state were performed with the MOLPRO quantum chemistry package using the internally contracted multireference configuration interaction method. This dipole moment function, along with the equilibrium constants calculated in this work, was used in the LEVEL program to calculate line strengths. The effect of vibration–rotation interaction on line strengths, known as the Herman–Wallis effect, was taken into account. The resulting line strengths were compiled into a new line list, which will aid in determining the abundance of CH in diverse astrophysical environments.

Unified Astronomy Thesaurus concepts: Spectral line lists (2082); Line intensities (2084); Molecular spectroscopic constants (2260); Interstellar molecules (849)

Materials only available in the online version of record: data behind figure, machine-readable table

1. Introduction

The CH radical, also known as the methylidyne radical, is a simple organic compound composed of a single hydrogen atom bonded to a carbon atom. CH was first identified by T. Heurlinger (1918). Since then, it has been extensively studied in part because of its astrophysical relevance. CH has been observed in numerous astrophysical environments and plays a crucial role in combustion, interstellar chemistry, and atmospheric reactions. In interstellar clouds, the formation of CH is believed to occur through a sequence of reactions initiated by the radiative association of C^+ with H_2, followed by dissociative recombination of CH_2^+ with electrons (J. Black & A. Dalgarno 1973). It is also an important tracer for molecular hydrogen in various interstellar environments, from diffuse clouds to high mass star formation regions (A. Danks et al. 1984; H. Wiesemeyer et al. 2018). Furthermore, CH can be used to determine the $^{12}C/^{13}C$ ratio throughout the Galaxy as it is ubiquitous, and ^{13}CH does not show a significant fractionation effect (A. M. Jacob et al. 2020).

CH has been detected in the Sun, stellar atmospheres, and interstellar clouds. It is observed through electronic transitions in the optical and ultraviolet regions, rotational and lambda-doubling transitions in the submillimeter and radio regions, as well as rovibrational transitions in the infrared region. A. McKellar (1940) identified CH in the interstellar medium (ISM) by three absorption lines from the $A^2\Delta$–$X^2\Pi$ and $B^2\Sigma^-$–$X^2\Pi$ transitions. This was the first observation of CH in the ISM and is considered one of the first molecules detected in the ISM. As of 2026 February, more than 340 molecules have been detected in the ISM or circumstellar shells (CDMS 2026). M. Nicolet (1938) identified the presence of CH in comets. Radio detection of CH in the ISM was achieved by O. Rydbeck et al. (1973) using the three hyperfine lines of the $^2\Pi_{1/2}$ lambda doublet transition near 3 GHz. J. Whiteoak et al. (1980) detected the 3264 MHz hyperfine transition of this lambda doublet in three external galaxies. N. Rangwala et al. (2014) observed submillimeter hyperfine lines of the 3/2–1/2 rotational transition in extragalactic sources. A. M. Jacob et al. (2020) detected ^{13}CH in the ISM and also calculated the $^{12}C/^{13}C$ ratio. I. Schroetter et al. (2025) detected rovibrational emission of the CH radical in the protoplanetary disk d203-506 with the James Webb Space Telescope.

Various techniques have been employed in the past to record high-resolution CH spectra in the laboratory. For instance, P. Bernath (1987) utilized an electrodeless quartz discharge tube driven by a microwave oscillator to obtain the vibration–rotation emission spectrum of the $X^2\Pi$ state of CH. M. Zachwieja (1995) recorded the $A^2\Delta$–$X^2\Pi$ band system of the CH radical from a Geissler tube using conventional spectroscopic methods. R. Engeln et al. (1999) employed cavity ring-down (CRD) absorption spectroscopy in an argon/acetylene plasma to capture rotationally resolved spectra of the $A^2\Delta$–$X^2\Pi$ transition of CH. P. Ghosh et al. (1999) produced the infrared bands of CH through a DC discharge of CH_4–He in a water-cooled cell and recorded spectra with a Fourier transform spectrometer (FTS). M. McCarthy et al. (2006) measured microwave lambda-doubling transitions of ^{12}CH and ^{13}CH in a discharge through methane or other hydrocarbons heavily diluted in a Ne buffer gas. M. Jackson et al. (2008) recorded far-infrared laser magnetic resonance spectra of CH by the reaction of fluorine atoms with methane in a flow system. C. Medcraft et al. (2019) used CRD UV spectroscopy to record the $C^2\Sigma^+$–$X^2\Pi$ transition of CH.

In addition to measurements with many ground-based observatories, CH has been detected from orbit, for example,

by the ATMOS instrument on Spacelab-3 (SL-3) (F. Mélen et al. 1989; M. Abrams et al. 1996), Atmospheric Chemistry Experiment Fourier Transform Spectrometer (ACE-FTS; F. Hase et al. 2010), Herschel Space Observatory (N. Rangwala et al. 2014), GREAT/SOFIA (A. M. Jacob et al. 2020), and JWST-Nirspec (I. Schroetter et al. 2025). Future space-based telescopes like the Nancy Grace Roman Space Telescope, Habitable Worlds Observatory, and LUVOIR, along with next-generation ground-based telescopes such as the Extremely Large Telescope (ELT), Thirty Meter Telescope (TMT), Square Kilometre Array (SKA), and Giant Magellan Telescope (GMT), are expected to provide further insights into the abundance of various molecules, including CH, in different sources. As high-resolution capabilities advance, the need for more accurate line lists, including precise line strengths, becomes increasingly important for detecting molecules like CH in a wide range of environments.

The CH radical is an open-shell molecule with one unpaired electron. The $X^2\Pi$ state is the ground electronic state with the principal electronic configuration $(1\sigma)^2(2\sigma)^2(3\sigma)^2(1\pi)^1$. The CH radical in the $X^2\Pi$ state is highly reactive and participates in chemical reactions through insertion or addition. The low-lying excited electronic states include doublets $A^2\Delta$, $B^2\Sigma^-$, and $C^2\Sigma^+$ states, along with a quartet $a^4\Sigma^-$ state. Numerous studies have investigated the electronic transitions of CH, including $A^2\Delta$–$X^2\Pi$ (M. Zachwieja 1995; R. Engeln et al. 1999), $B^2\Sigma^-$–$X^2\Pi$ (P. Bernath et al. 1991; R. Kepa et al. 1996), $C^2\Sigma^+$–$X^2\Pi$ (X. Li et al. 1999), as well as its rovibrational transition $X^2\Pi$–$X^2\Pi$ (P. Bernath 1987; R. Colin & P. F. Bernath 2010; T. Masseron et al. 2014). This study focuses specifically on the rovibrational $X^2\Pi$–$X^2\Pi$ transitions of CH. P. Bernath (1987) analyzed the 1–0, 2–1, and 3–2 vibrational bands of the $X^2\Pi$–$X^2\Pi$ transition. F. Mélen et al. (1989) extended Bernath's analysis to higher rotational levels and also included the analysis of the 4–3 vibrational band, using solar absorption spectra obtained from orbit with the ATMOS SL-3 instrument. P. Bernath et al. (1991) recorded the emission spectra of the $A^2\Delta$–$X^2\Pi$ and $B^2\Sigma^-$–$X^2\Pi$ electronic transitions and integrated their analysis with the vibration–rotation transitions. They also utilized the ATMOS SL-3 spectra to include higher rotational levels and provided updated spectroscopic constants. R. Colin & P. F. Bernath (2010) extended the analysis to the 5–4 vibrational band and assigned several new lines (primarily P and Q branches) to previously analyzed bands. T. Masseron et al. (2014) compiled all previous data concerning the $X^2\Pi$–$X^2\Pi$, $A^2\Delta$–$X^2\Pi$, $B^2\Sigma^-$–$X^2\Pi$, and $C^2\Sigma^+$–$X^2\Pi$ transitions, providing updated constants and a line list for both ^{12}CH and ^{13}CH. T. Furtenbacher et al. (2022) conducted a MARVEL analysis to provide energy levels with individual uncertainties.

In this study, a reanalysis of the 4–3 and 5–4 vibrational bands of the CH $X^2\Pi$–$X^2\Pi$ transition is carried out, and new spectroscopic constants for the $v = 4$ and $v = 5$ levels are determined. For this analysis, we utilized a new solar absorption spectrum obtained from ACE-FTS and an emission spectrum of CH recorded by P. Bernath (1987). Additionally, line strengths have been calculated considering the Herman–Wallis (H-W) effect to account for the rotational dependencies of line strengths.

2. Methods

2.1. Ab Initio Calculations

The permanent dipole moment (PDM) function was calculated with the MOLPRO quantum chemistry package (H. Werner et al. 2011; H.-J. Werner et al. 2020, 2022) using the internally contracted multireference configuration interaction method (MRCI; H.-J. Werner & P. J. Knowles 1988). Complete active space self-consistent field calculations (CASSCF; H.-J. Werner & P. J. Knowles 1985; D. A. Kreplin et al. 2019) were performed to optimize the molecular orbitals (MOs) used in the MRCI calculations. The correlation consistent basis set aug-cc-pV6Z (T. H. Dunning 1989; D. E. Woon & T. H. Dunning 1994; B. P. Pritchard et al. 2019) was used for the hydrogen atom, and aug-cc-pCV5Z (T. H. Dunning 1989; B. P. Pritchard et al. 2019) for the carbon atom. Calculations were performed within the C_{2v} symmetry point group with six occupied orbitals (4 A_1, 1 B_1, 1 B_2, 0 A_2). In the CASSCF calculation, one orbital belonging to the A_1 representation was doubly occupied in all configurations (corresponding to the 1 s orbital of the carbon atom), leaving three A_1, one B_1, and one B_2 orbitals for the five active electrons. This active space was chosen because it provides good convergence of the molecular orbitals and ensures a smooth, continuous behavior of the solution as a function of bond length. In the MRCI calculations, the same active space was used, but excitations from the 1 s orbital of C were allowed. The Davidson (relaxed reference) and Douglas–Kroll corrections were used to calculate the equilibrium parameters.

Figure 1 shows our PDM and compares it with the literature calculations. All calculations shown agree to within 0.05. D. Z. Hou & L. Liu (2024) used aug-cc-pV(5+d)Z basis set for the carbon atom and aug-cc-pV5Z for the hydrogen atom. J. Cui et al. (2018) also used aug-cc-pV5Z for the hydrogen atom but aug-cc-pCV5Z for the carbon atom. Both articles used state-averaged CASSCF orbitals in their MRCI calculations, whereas we optimized our orbitals only for the $X^2\Pi$ state. Positive PDM corresponds to a C^-H^+ dipole. As explained in G. C. Lie et al. (1973a) and G. C. Lie et al. (1973b), a C^-H^+ configuration is more stable at large bond lengths, which is why the PDM goes to negative values.

From our theoretical calculation, an equilibrium bond length of 1.1178 Å was obtained, which is closer to the experiment (1.1197796(63) Å in this work) compared to the theoretical value of Z. Hou & L. Liu (2024) obtained with state-averaged orbitals (1.10 Å). D. H. Phelps & F. W. Dalby (1966) observed the Stark splitting in the level $J = \frac{1}{2}$ and found a PDM at equilibrium bond length of 1.46(6) D. We obtain from our calculation a value of 1.4139 D, which agrees within experimental uncertainty.

2.2. Spectral Fitting

Our analysis uses the widely used spectral fitting software PGOPHER (C. M. Western 2017), which utilizes the standard N^2 Hamiltonian to describe molecular energy levels. Here, $\boldsymbol{N} = \boldsymbol{J} - \boldsymbol{S}$ is the rotational angular momentum that excludes the contribution from electron spin. The effective Hamiltonian ($H_{\rm eff}$) for the $X^2\Pi$ state is the sum of rotational ($H_{\rm rot}$), spin–orbit coupling ($H_{\rm so}$), spin-rotation term ($H_{\rm sr}$), and lambda doubling term ($H_{\rm ld}$). A detailed description of each term of the effective Hamiltonian is provided in C. M. Western (2017).

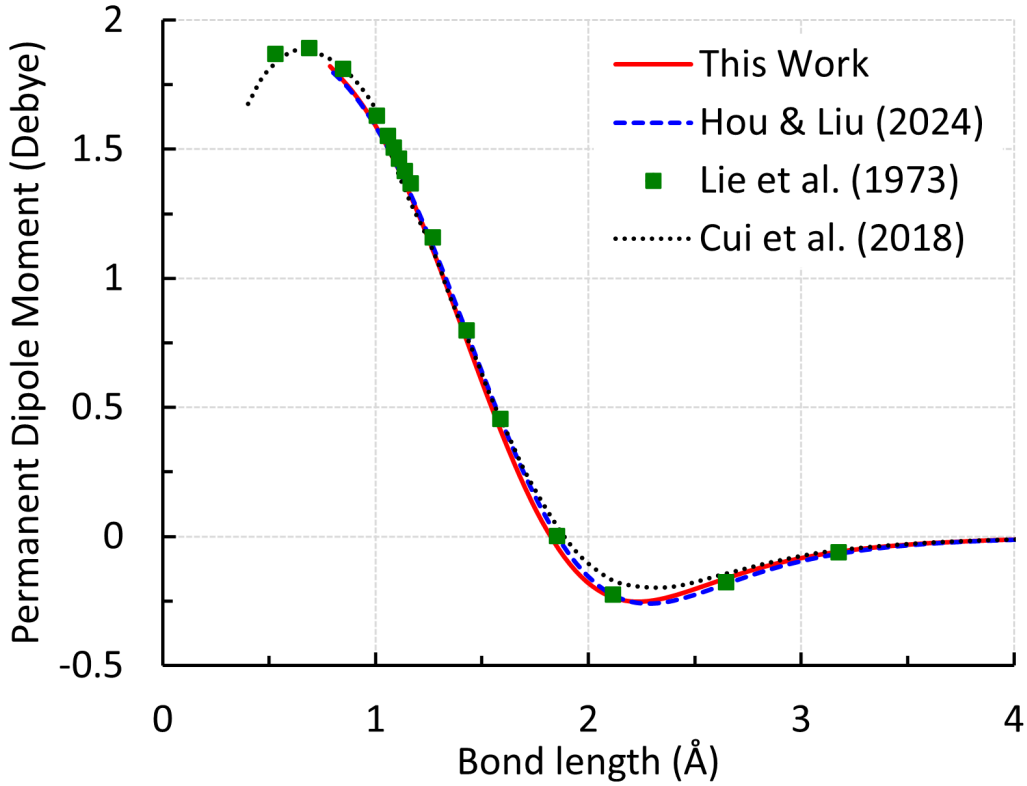

Figure 1. Permanent dipole moment function calculated in this work with CASSCF(4110)/MRCI and 1 s correlation of the C atom (red curve) compared with calculations from Z. Hou & L. Liu (2024; blue dashed curve), G. C. Lie et al. (1973b; green squares), and J. Cui et al. (2018; black dotted curve). (The data used to create this figure are available in the online article.)

The spectrum used in this analysis is the newly obtained solar absorption infrared spectrum obtained by the ACE-FTS instrument on board the Canadian SCISAT satellite. The ACE-FTS has a resolution of 0.02 cm^{-1}, with coverage from 750 to 4400 cm^{-1} and uses InSb and HgCdTe (MCT) detectors. All high Sun data were employed in the average, including both opportunistic sets of high Sun measurements and high Sun measurements collected as reference spectra for calibrating atmospheric measurements. Filters were applied to remove spectra where the signal was unexpectedly high or low, where noise levels were excessive, and where weak atmospheric CO_2 lines were observed in the spectrum, in occultations where CO_2 absorption extended above 160 km. To avoid artificially broadening lines in the spectrum, each measurement was "stretched" in wavenumber to align with a spectrally calibrated reference spectrum using three window regions to determine the amount of stretching required on the wavenumber scale: 2375–2376.6 cm^{-1}, 2437.4–2438.1 cm^{-1}, and 2695.7–2696.6 cm^{-1}. CO solar features were used for wavenumber calibration of the reference spectrum to ensure the final average spectrum had the proper wavenumber calibration.

The spectrum analyzed here is the average of spectra with both high and low solar activity, which do not show a detectable difference despite variations in solar activity. The new spectrum analyzed in this study incorporates data from the InSb detector only, covering a wavenumber range of 1829.40–4439.88 cm^{-1}. 3,069,142 individual spectra were used for constructing the new solar spectrum, while the previous version of the ACE-FTS solar atlas was based on 224,782 measurements. To improve the quality of the raw measured InSb spectrum, channeling effects that cause ripples in the baseline were eliminated. As for the previous version of the ACE-FTS solar atlas, the channeling frequencies were identified in the Fourier domain, and the same approach for channeling removal was used. Despite the significantly improved noise level of the new spectrum, no additional frequency ranges suffering from channeling contamination beyond those previously identified (see Table 2 in F. Hase et al. 2010) were found in the InSb spectral range. As for the previous version of the atlas, a smooth spectral response function of the spectrometer has been constructed and was divided off for generating a solar transmission spectrum with the background continuum radiance level normalized to unity.

Additionally, the spectrum was apodized using a Gaussian apodization to approximately reproduce the resulting solar line shapes of the previously published version. The spectral calibration was adjusted by applying a spectral stretch to match the calibration of the previous atlas. Data from the MCT detector is currently being prepared and will be published with a new solar atlas that is also in development. Compared to the old ACE-FTS solar absorption spectrum (R. Colin & P. F. Bernath 2010; F. Hase et al. 2010; T. Masseron et al. 2014), the new ACE-FTS solar spectrum is improved in some regions. In particular, certain weak features located between strong lines are now more distinctly resolved, and the CO overtone region shows substantial enhancement over the older version. The solar spectrum used in the analysis is available on Zenodo at doi:10.5281/zenodo.19916162.

We also incorporated the emission spectrum recorded by P. Bernath (1987) in our analysis. This spectrum was useful for assigning additional lines, especially for low-J transitions, while the solar spectrum was more effective for high-J transitions. Thus, both the solar spectrum and the laboratory

Table 1
Spectroscopic Constants for Different Vibrational Levels of $X^2\Pi$ State of ^{12}CH

Constant	$v = 0$	$v = 1$	$v = 2$	$v = 3$	$v = 4$	$v = 5$
T_v	0	2732.9784(11)	5339.90410(161)	7822.21922(199)	10180.99981(231)	12416.7960(32)
A	28.14675[a]	28.33833[a]	28.615(57)	28.766(50)	28.986(44)	29.241(49)
B	14.1923826(657)	13.6617664(562)	13.1357733(533)	12.6134002(524)	12.0929612(562)	11.572894(125)
$D \times 10^3$	1.461070(403)	1.437255(333)	1.415255(330)	1.395800(341)	1.378852(359)	1.36925(142)
$H \times 10^7$	1.09982(800)	1.05402(911)	1.0109(104)	0.9686(109)	0.9088(106)	0.8867(446)
$L \times 10^{12}$	−1.77(192)	−2.86(176)	−4.35(159)	−6.40(140)	−8.36(120)	...
γ	−0.028854(926)	−0.026825(918)	−0.024970(897)	−0.023541(873)	−0.021794(862)	−0.019387(988)
p	0.034160(378)	0.032202(352)	0.030986(356)	0.029387(381)	0.02815(45)	0.02795(99)
q	0.0386654(334)	0.0372860(297)	0.0359245(316)	0.0345401(344)	0.0331701(389)	0.032026(138)
$p_D \times 10^5$	−0.508(394)	−0.406(365)	−0.356(338)	−0.285(311)	−0.301(282)	−1.43(66)
$q_D \times 10^5$	−1.5765(208)	−1.5356(227)	−1.4943(245)	−1.4452(248)	−1.3939(241)	−1.658(199)
$q_H \times 10^8$	0.3686(605)	0.346(556)	0.3257(505)	0.3034(447)	0.2669(385)	1.326(688)
$\gamma_D \times 10^5$	1.819(264)	1.671(245)	1.563(227)	1.525(210)	1.377(191)	1.11(41)

Notes. All the values are in cm^{-1}. One standard deviation error is given in parentheses.
[a] These values were fixed to M. Jackson et al. (2008).

spectrum played complementary roles in line assignment. This is because the laboratory spectra are moderately hot, resulting in low J levels being more populated and better resolved due to narrower Doppler widths. Conversely, in the solar spectrum, high J levels are more populated because of the Sun's hotter atmosphere. Most of the high-J transitions present in the solar spectrum were either weak or entirely absent in the laboratory spectrum.

3. Results

3.1. Spectroscopic Constants

Previous high-resolution studies have examined the $X^2\Pi$–$X^2\Pi$ rovibrational transitions of CH up to the 5–4 vibrational band (R. Colin & P. F. Bernath 2010; T. Masseron et al. 2014). For the bands up to the 4–3 vibrational band, all P, Q, and R branch transitions have been identified. In contrast, the 5–4 band contains only R branch lines, with a maximum rotational assignment of $J_{max} = 11.5$. These limitations point to two clear areas for improvement: (i) inclusion of P and Q branch transitions in the 5–4 band, and (ii) extension of J assignments to higher values.

In an attempt to improve the constants for $v = 4$ and $v = 5$ levels of the $X^2\Pi$ state, we have assigned some new lines to the 4–3 and 5–4 vibrational bands of the $X^2\Pi$–$X^2\Pi$ transition. At first, we assigned some P and Q branch lines to the 4–3 band by floating some of the constants of the $v = 4$ level with the constants for the $v = 3$ level fixed. Then, we floated $v = 5$ level constants to fit additional lines on the 5–4 vibrational band. Mostly, the new assignments in the 5–4 band are R lines as they were distinct and easy to identify. Unfortunately, the P and Q branches of the 5–4 vibrational band are concealed by the intense CO lines in the solar spectrum, making it challenging to fit these branches. Despite this, we fitted a few P and Q lines of the 5–4 band. We believe that these additional lines have improved the reliability of the constants for the $v = 4$ and $v = 5$ levels. We adjusted all constants up to $v = 3$ (except for A for $v = 0$ and 1) after assigning additional lines in the 5–4 and 4–3 vibrational transitions. Since each transition connects a vibrational level to the one just below it, the constants for $v \leqslant 3$ have changed slightly compared to those reported by R. Colin & P. F. Bernath (2010), mostly remaining within the error limits. The updated constants for $v \leqslant 5$ are reported in Table 1. We attempted to fit the 6–5 vibrational band; however, this was not possible as all P, Q, and R lines of this band were completely hidden by the intense CO lines.

Some of the assigned 5–4 rovibrational lines are shown in Figure 2. Note that in Figure 2 and in all other figures containing the solar spectrum, the atmospheric transmittance values were subtracted from 1 to show the spectral lines upward. The lines depicted in pink represent the assigned lines, while the dark red lines illustrate the ACE-FTS solar absorption spectrum. The list of newly assigned lines and their corresponding residuals is presented in Table 2. This table shows the new lines along with their observed and calculated positions, as well as the differences between them. Additionally, we provide a comprehensive log file that includes all the lines previously analyzed by R. Colin & P. F. Bernath (2010), along with the newly assigned lines in MRT format as supplementary material.

3.2. Equilibrium Constants

After refining the line positions, the next step was to optimize the accuracy of the line strengths. For light molecules like CH, vibration–rotation coupling creates a significant dependence on the quantum number J for line strengths through the H-W effect (R. Herman & R. F. Wallis 1955). This effect enhances the intensities of P-branch lines while reducing the intensities of R-branch lines, or vice versa.

The spectroscopic constants from Table 1, along with Equations (1), (2), and (3) from P. F. Bernath (2025), were used to calculate the equilibrium constants. The equilibrium constants for the $X^2\Pi$ state of ^{12}CH are shown in Table 3. The table also displays the equilibrium bond length (r_e) calculated in this work using the relation $r_e = \left(\frac{16.857629192}{\mu B_e \text{ cm}^{-1}}\right)^{1/2}$. The atomic masses of carbon (C) and hydrogen (H) were obtained from the AMDC website[5] for this calculation. The equilibrium constants calculated by R. Colin & P. F. Bernath (2010) and T. Masseron et al. (2014) are also provided in the table for comparison. The errors in the parentheses represent statistical

[5] https://www-nds.iaea.org/amdc/ame2020/mass_1.mas20.txt

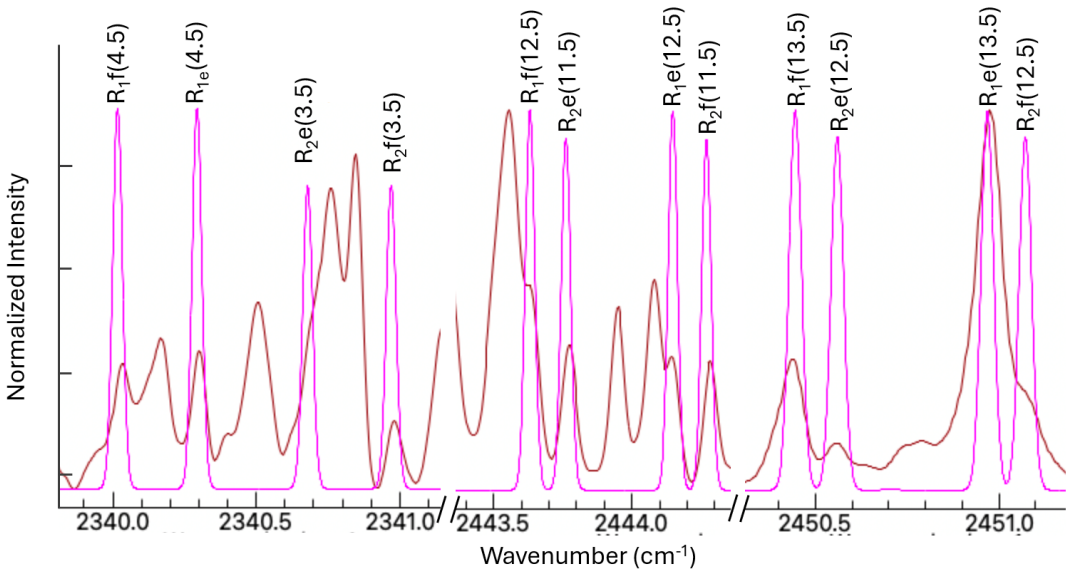

Figure 2. New assignments made in the 5–4 band of the $X^2\Pi$–$X^2\Pi$ transition of CH. The maroon color represents the emission spectra recorded by ACE-FTS, while the pink color represents the simulated lines obtained using the PGOPHER program. Each line is labeled with its branch name, spin component, parity, and rotational quantum number.

uncertainties only and do not include the systematic errors:

$$G_v = \omega_e\left(v+\frac{1}{2}\right) - \omega_e x_e\left(v+\frac{1}{2}\right)^2 + \omega_e y_e\left(v+\frac{1}{2}\right)^3 + \ldots \quad (1)$$

$$B_v = B_e - \alpha_e\left(v+\frac{1}{2}\right) + \gamma_e\left(v+\frac{1}{2}\right)^2 + \ldots \quad (2)$$

$$D_v = D_e + \beta_e\left(v+\frac{1}{2}\right) + \ldots \quad (3)$$

3.3. Line Intensity

The equilibrium constants determined in this study were used in Le Roy's RKR1 program (R. J. Le Roy 2017a) to generate potential energy curves. The output from the RKR1 program was then utilized in the LEVEL program (R. J. Le Roy 2017b), along with the PDM calculated in this study, to determine the line strengths. Figure 3 illustrates the potential energy curve for the $X^2\Pi$ state of CH, along with the vibrational wave functions for the $v = 0$–5 levels. The potential energy curve was derived from the output of the RKR1 program, while the vibrational wave functions were obtained from the LEVEL program.

The LEVEL program does not include electron spin and so provides electric dipole matrix elements expressed in terms of N. However, the PGOPHER program requires that these matrix elements be expressed in terms of J. Thus, it is essential to convert the N-dependent matrix elements from Hund's coupling case (b) to J-dependent form in Hund's case (a). We used the conversion method described by J. S. Brooke et al. (2016) for this purpose. For details on how to convert from Hund's case (b) to case (a), we refer readers to J. S. Brooke et al. (2016). After converting from Hund's case (b) to case (a), the resulting dipole matrix elements were entered into the PGOPHER program in tabular format. PGOPHER then generates a line list with line strengths, which is provided as supplementary material in machine-readable table (MRT) format. The line list contains the Einstein A values. We then converted the Einstein A values into oscillator strengths ($f_{J'\leftarrow J''}$) using the relation provided by P. F. Bernath (2025):

$$f_{J'\leftarrow J''} = \frac{1.499194}{\tilde{\nu}^2}\frac{2J'+1}{2J''+1}A_{J'\rightarrow J''} \quad (4)$$

with $\tilde{\nu}$ in cm^{-1}. We also calculated the radiative lifetime of ^{12}CH in different vibrational levels of the $X^2\Pi$ state using the relation $\tau_{v'} = \frac{1}{\sum_{v''}A_{v'\rightarrow v''}}$. In this relation, $A_{v'\rightarrow v''} = 3.1361889 \times 10^{-7}\tilde{\nu}^3\mu^2_{v'\rightarrow v''}$ (P. F. Bernath 2025) are the Einstein A values with $\tilde{\nu}$ in cm^{-1} and μ in debye. The calculated lifetimes are shown in Table 4.

A comparison of the Einstein A values for the spectral lines that include the H-W effect versus those that do not is presented in Figure 4. The figure illustrates that the change in Einstein A values is small for low rotational quantum numbers (J) but increases significantly for higher J values. For the P branch lines, the percentage change in the Einstein A values initially decreases with increasing J and then starts to rise. In contrast, for the R branch lines, the percentage change in the Einstein A values shows a significant increase with J, although there is a slight decrease at high J values for the 4–3 and 5–4 bands. The maximum decrease in Einstein A values for the P lines, after incorporating the H-W effect, is 24.43%, while the maximum increase for the R lines is 201.27%. The figure specifically displays data for the F_1 component and the "e" parity levels, as the percentage increase in values for the F_2 components and "f" levels is identical. This consistency arises because the LEVEL program treats all states as singlet states. The line intensities generated by the LEVEL program depend solely on the J values and branches for each vibrational level; they do not vary based on the spin components and parities. It is important to note that the Einstein A values for transitions with different spin components and parities differ; however, the percentage change after incorporating the H-W effect for these transitions remains the same.

Table 2
List of New Lines and Residuals Assigned in This Work for the ^{12}CH $X^2\Pi$–$X^2\Pi$ Transition from the PGOPHER Log File

J'	P'	J''	P''	Obs.	Calc.	Obs.–Calc.	Line Assignment
2.5	e	1.5	e	2303.1396	2303.1371	0.0025	rR2e(1.5) : v = 5 2.5 3 F2e—v = 4 1.5 2 F2e
1.5	e	1.5	f	2232.7175	2232.7134	0.0041	qQ2f(1.5) : v = 5 1.5 2 F2e—v = 4 1.5 2 F2f
1.5	f	1.5	e	2233.0889	2233.098	−0.0091	qQ2e(1.5) : v = 5 1.5 2 F2f—v = 4 1.5 2 F2e
2.5	f	1.5	f	2303.3259	2303.3329	−0.007	rR2f(1.5) : v = 5 2.5 3 F2f—v = 4 1.5 2 F2f
1.5	e	2.5	e	2187.2564	2187.2608	−0.0044	pP1e(2.5) : v = 5 1.5 1 F1e—v = 4 2.5 2 F1e
2.5	f	2.5	e	2230.105	2230.1013	0.0037	qQ2e(2.5) : v = 5 2.5 3 F2f—v = 4 2.5 3 F2e
1.5	f	2.5	f	2187.3786	2187.3856	−0.007	pP1f(2.5) : v = 5 1.5 1 F1f—v = 4 2.5 2 F1f
3.5	e	2.5	e	2322.2974	2322.298	−0.0006	rR2e(2.5) : v = 5 3.5 4 F2e—v = 4 2.5 3 F2e
2.5	f	2.5	e	2232.3882	2232.4071	−0.0189	qQ1e(2.5) : v = 5 2.5 2 F1f—v = 4 2.5 2 F1e
2.5	e	2.5	f	2232.6647	2232.6552	0.0095	qQ1f(2.5) : v = 5 2.5 2 F1e—v = 4 2.5 2 F1f
3.5	f	2.5	f	2301.2583	2301.2468	0.0115	rR1f(2.5) : v = 5 3.5 3 F1f—v = 4 2.5 2 F1f
3.5	e	2.5	e	2301.427	2301.4147	0.0123	rR1e(2.5) : v = 5 3.5 3 F1e—v = 4 2.5 2 F1e
3.5	f	2.5	f	2322.5554	2322.5468	0.0086	rR2f(2.5) : v = 5 3.5 4 F2f—v = 4 2.5 3 F2f
2.5	e	2.5	f	2229.2954	2229.2975	−0.0021	qQ2f(2.5) : v = 5 2.5 3 F2e—v = 4 2.5 3 F2f
3.5	e	3.5	f	2347.7707	2347.7677	0.003	qQ2f(3.5) : v = 4 3.5 4 F2e—v = 3 3.5 4 F2f
4.5	e	3.5	e	2340.7002	2340.6895	0.0107	rR2e(3.5) : v = 5 4.5 5 F2e—v = 4 3.5 4 F2e
4.5	e	3.5	e	2321.5065	2321.5046	0.0019	rR1e(3.5) : v = 5 4.5 4 F1e—v = 4 3.5 3 F1e
4.5	f	3.5	f	2321.2706	2321.2819	−0.0113	rR1f(3.5) : v = 5 4.5 4 F1f—v = 4 3.5 3 F1f
3.5	e	3.5	f	2229.7507	2229.7559	−0.0052	qQ1f(3.5) : v = 5 3.5 3 F1e—v = 4 3.5 3 F1f
3.5	f	3.5	e	2229.1561	2229.1468	0.0093	qQ1e(3.5) : v = 5 3.5 3 F1f—v = 4 3.5 3 F1e
4.5	f	3.5	f	2340.9804	2340.9881	−0.0077	rR2f(3.5) : v = 5 4.5 5 F2f—v = 4 3.5 4 F2f
3.5	f	3.5	e	2349.1723	2349.1731	−0.0008	qQ2e(3.5) : v = 4 3.5 4 F2f—v = 3 3.5 4 F2e
5.5	e	4.5	e	2340.301	2340.3037	−0.0027	rR1e(4.5) : v = 5 5.5 5 F1e—v = 4 4.5 4 F1e
4.5	f	4.5	e	2347.715	2347.7316	−0.0166	qQ1e(4.5) : v = 4 4.5 4 F1f—v = 3 4.5 4 F1e
4.5	e	4.5	f	2342.2152	2342.2054	0.0098	qQ2f(4.5) : v = 4 4.5 5 F2e—v = 3 4.5 5 F2f
4.5	e	4.5	f	2348.8796	2348.8791	0.0005	qQ1f(4.5) : v = 4 4.5 4 F1e—v = 3 4.5 4 F1f
4.5	f	4.5	e	2344.2987	2344.3028	−0.0041	qQ2e(4.5) : v = 4 4.5 5 F2f—v = 3 4.5 5 F2e
3.5	f	4.5	f	2104.7678	2104.7624	0.0054	pP2f(4.5) : v = 5 3.5 4 F2f—v = 4 4.5 5 F2f
3.5	e	4.5	e	2105.1242	2105.1287	−0.0045	pP2e(4.5) : v = 5 3.5 4 F2e—v = 4 4.5 5 F2e
4.5	f	5.5	f	2105.4648	2105.4539	0.0109	pP1f(5.5) : v = 5 4.5 4 F1f—v = 4 5.5 5 F1f
4.5	e	5.5	e	2105.1242	2105.1176	0.0066	pP1e(5.5) : v = 5 4.5 4 F1e—v = 4 5.5 5 F1e
5.5	f	5.5	e	2338.4725	2338.4668	0.0057	qQ2e(5.5) : v = 4 5.5 6 F2f—v = 3 5.5 6 F2e
5.5	e	5.5	f	2344.0008	2344.0139	−0.0131	qQ1f(5.5) : v = 4 5.5 5 F1e—v = 3 5.5 5 F1f
5.5	f	5.5	e	2342.2152	2342.2318	−0.0166	qQ1e(5.5) : v = 4 5.5 5 F1f—v = 3 5.5 5 F1e
6.5	f	5.5	f	2504.7989	2504.7797	0.0192	rR2f(5.5) : v = 4 6.5 7 F2f—v = 3 5.5 6 F2f
5.5	e	5.5	f	2335.5453	2335.5525	−0.0072	qQ2f(5.5) : v = 4 5.5 6 F2e—v = 3 5.5 6 F2f
6.5	f	6.5	e	2335.6298	2335.6307	−0.0009	qQ1e(6.5) : v = 4 6.5 6 F1f—v = 3 6.5 6 F1e
6.5	e	6.5	f	2338.1673	2338.1726	−0.0053	qQ1f(6.5) : v = 4 6.5 6 F1e—v = 3 6.5 6 F1f
8.5	f	9.5	f	2064.8949	2064.8977	−0.0028	pP2f(9.5) : v = 4 8.5 9 F2f—v = 3 9.5 10 F2f
8.5	e	9.5	e	2065.6748	2065.6739	0.0009	pP2e(9.5) : v = 4 8.5 9 F2e—v = 3 9.5 10 F2e
9.5	e	10.5	e	2064.9944	2064.9995	−0.0051	pP1e(10.5) : v = 4 9.5 9 F1e—v = 3 10.5 10 F1e
9.5	f	10.5	f	2031.1117	2031.1091	0.0026	pP2f(10.5) : v = 4 9.5 10 F2f—v = 3 10.5 11 F2f
9.5	f	10.5	f	2065.7472	2065.7353	0.0119	pP1f(10.5) : v = 4 9.5 9 F1f—v = 3 10.5 10 F1f
9.5	e	10.5	e	2031.9646	2031.9624	0.0022	pP2e(10.5) : v = 4 9.5 10 F2e—v = 3 10.5 11 F2e
12.5	e	11.5	e	2443.7719	2443.7697	0.0022	rR2e(11.5) : v = 5 12.5 13 F2e—v = 4 11.5 12 F2e
12.5	f	11.5	f	2444.2849	2444.28	0.0049	rR2f(11.5) : v = 5 12.5 13 F2f—v = 4 11.5 12 F2f
10.5	e	11.5	e	2031.1915	2031.1969	−0.0054	pP1e(11.5) : v = 4 10.5 10 F1e—v = 3 11.5 11 F1e
10.5	f	11.5	f	2032.0121	2032.0088	0.0033	pP1f(11.5) : v = 4 10.5 10 F1f—v = 3 11.5 11 F1f
13.5	e	12.5	e	2444.1447	2444.1506	−0.0059	rR1e(12.5) : v = 5 13.5 13 F1e—v = 4 12.5 12 F1e
13.5	f	12.5	f	2443.6289	2443.6362	−0.0073	rR1f(12.5) : v = 5 13.5 13 F1f—v = 4 12.5 12 F1f
13.5	e	12.5	e	2450.5574	2450.5576	−0.0002	rR2e(12.5) : v = 5 13.5 14 F2e—v = 4 12.5 13 F2e
13.5	f	12.5	f	2451.0691	2451.0761	−0.007	rR2f(12.5) : v = 5 13.5 14 F2f—v = 4 12.5 13 F2f
14.5	e	13.5	e	2450.9759	2450.9657	0.0102	rR1e(13.5) : v = 5 14.5 14 F1e—v = 4 13.5 13 F1e
14.5	f	13.5	f	2450.4377	2450.436	0.0017	rR1f(13.5) : v = 5 14.5 14 F1f—v = 4 13.5 13 F1f

Note. J is the total angular momentum, P is the e/f parity, Obs. is the observed line position in cm^{-1}, Calc. is the calculated line position in cm^{-1}, and Obs.–Calc. is the observed minus calculated line position in cm^{-1}.

(This table is available in its entirety in machine-readable form in the online article.)

The line intensities of the simulated spectrum that includes the H-W effect are compared with the ACE-FTS solar spectrum in Figure 5. The blue spectrum shows the simulation including the H-W effect, while the dark red spectrum represents the solar spectrum. In Figure 5, the CH lines are normalized by dividing the simulated line intensities by the intensity of an R line at 2716.83 cm^{-1}. This specific R line was selected because it is located in a clean region of the

Table 3
Equilibrium Constants for the $X^2\Pi$ State of ^{12}CH

Constant	This Work	Previous Works
ω_e	2860.873(80)	2860.88(5)[a], 2860.9238[b]
$\omega_e x_e$	64.541(54)	64.55(5)[a], 64.58180[b]
$\omega_e y_e$	0.395(13)	0.40(1)[a], 0.407275[b]
$\omega_e z_e$	−0.0186(11)	−0.019(1)[a], −0.01980[b]
B_e	14.46005(16)	14.45004(4)[a], 14.45924[b]
α_e	0.53699(24)	0.53502[b]
$\gamma_e \times 10^3$	3.531(94)	1.993[b]
$\delta_e \times 10^4$	2.44(10)	2.14[b]
$D_e \times 10^3$	1.4656(42)	1.4759(4)[a]
$\beta_e \times 10^5$	1.87(12)	…
r_e	1.1197796(63)	1.11981[b]

Notes. The equilibrium constants for the $X^2\Pi$ state of CH, calculated using spectroscopic constants from R. Colin & P. F. Bernath (2010) and this work, are shown in the above table. One standard deviation error is given in parentheses. The bond length (r_e) is in Å, and all other values are in cm^{-1}.
[a] R. Colin & P. F. Bernath (2010).
[b] T. Masseron et al. (2014).

spectrum. Each line is labeled with its vibrational band (v'–v''), followed by branch, parity, and lower state rotational quantum number (J). The line intensities incorporating the H-W effect align well with the solar spectrum, particularly for those lines that are distinct and unblended. In Figure 6, we compare the line intensities with and without the H-W effect against the absorption solar spectrum recorded by ACE-FTS. The normalization of the CH lines was performed in the same way as in Figure 5. The simulated spectrum with the H-W effect is represented in blue, the simulated spectrum without the H-W effect is in orange, and the ACE-FTS solar absorption spectrum is shown in dark red. The simulation without the H-W effect includes band strength from the LEVEL output, which does not account for the H-W effect. Although not perfect, the line intensities that include the H-W effect match the solar spectrum more closely than those that do not.

4. Discussion

Ground-based infrared measurements of astronomical sources are difficult, as the light is contaminated by absorption from the Earth's atmosphere. This requires observations from high altitudes, particularly from space. While measurements from high-flying aircraft or balloons offer some solutions, they still do not completely eliminate telluric absorption. NASA's ATMOS instrument on the Space Shuttle captured the Sun's high-resolution infrared spectrum (M. Abrams et al. 1996), later improved by ACE-FTS on SCISAT, which achieved a higher signal-to-noise ratio (F. Hase et al. 2010). A new version of the ACE-FTS solar absorption spectrum recorded with an InSb detector is used in this work.

The $X^2\Pi$–$X^2\Pi$ transition of the CH molecule exhibits prominent features in the infrared region. The $X^2\Pi$ state of CH belongs to Hund's case (b), so N ($\boldsymbol{N} = \boldsymbol{J} - \boldsymbol{S}$) is a useful quantum number with rotational energy levels described approximately by $BN(N+1)$ (P. F. Bernath 2025). Each N value is split into two components, F_1 and F_2, where F_1 levels correspond to $N = J - \frac{1}{2}$ and F_2 levels correspond to $N = J + \frac{1}{2}$. Since the spin–orbit coupling constant (A) is positive, F_1 levels are lower in energy relative to F_2 levels for each N. Lambda doubling further splits F_1 and F_2 into F_{1e}, F_{1f} and F_{2e}, F_{2f}. Each vibrational band has P, Q, and R branches, and the order of intensities is R > P > Q.

T. Masseron et al. (2014) calculated the N-dependent dipole matrix elements using the LEVEL program. To convert these N-dependent matrix elements to a J-dependent form, as required by PGOPHER, they fitted a polynomial of order n, where the value of n was chosen to ensure that the rms error of the fit was less than 1%. This method works because the ground state of CH belongs to Hund's case (b). In contrast, this work utilizes a different method to change from N-dependent to J-dependent dipole matrix elements. Specifically, we utilized a method developed by Brooke (translated into Python), which has been used in several previous studies (J. S. Brooke et al. 2016). The results obtained from these two methods are compared in Figure 7. As depicted in the figure, the two methods mostly agree for all the vibrational bands, with minor differences for some J values.

A comparison between the line positions and gf values calculated in this work and those from T. Masseron et al. (2014) was performed. The line positions agree well across all vibrational bands, with the median differences below 0.01 cm^{-1} for 1–0 through 4–3 bands. The 5–4 band shows a slightly larger deviation of 0.014 cm^{-1}, but this is expected as the line positions were updated for the 5–4 band. The gf value is the product of statistical weight ($g = 2J'' + 1$) and the oscillator strength (f), representing the probability of a transition between two energy levels. A plot of differences in $\log_{10}(gf)$ between this work and T. Masseron et al. (2014) as a function of rotational quantum number of the lower state (J'') across all vibrational bands is shown in Figure 8. The plot shows that the gf values calculated in this work were found slightly larger than those calculated by T. Masseron et al. (2014). The average difference of the $\log_{10}(gf)$ values from this work and T. Masseron et al. (2014) increases from about 0.0172 for the 1–0 band to 0.0313 for the 5–4 band. Similarly, the average ratio of the gf values rises from 1.041 for the 1–0 band to 1.075 for the 5–4 band, indicating that the discrepancy increases with increasing vibrational level. For the same vibrational band, the disagreement is largest at low J and decreases toward high J, producing the smooth, wavelike pattern seen in the figure. This discrepancy is consistent across all three rotational branches. The differences are expected because the methodologies used to calculate the line strengths differ between the two studies, and the spectroscopic constants and PDMs used to calculate them are updated in this work.

The discrepancies in the intensities between the observed solar spectrum and the simulated spectrum can arise from multiple sources. To normalize the spectra, the intensity of an R line is chosen, and any error in this normalization propagates into all relative intensity comparisons. The spectroscopic constants used are based on fitting of rotational lines up to a limited J, meaning they may carry inaccuracies at higher J values, and Rydberg–Klein–Rees (RKR) potential energy surfaces derived from these constants and used in the LEVEL program may not give accurate band strengths across all vibrational levels. Similarly, the calculated dipole moment functions used in the calculation may have uncertainties that directly affect transition strengths even after applying the H-W correction. Additionally, several instrumental and modeling factors like apodization errors, finite resolution, phase errors, line shape treatments, etc., may cause the observed discrepancies.

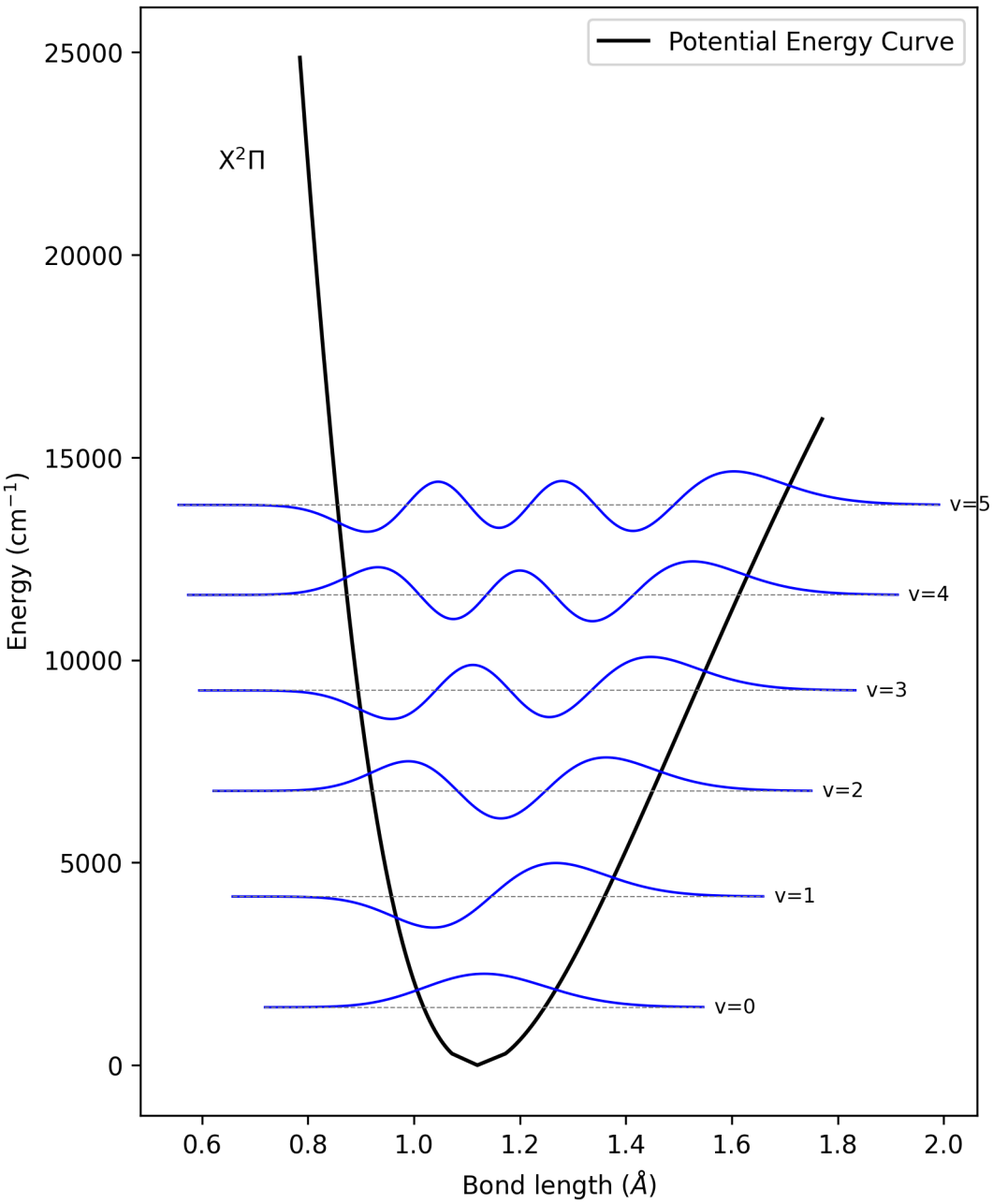

Figure 3. Plot of the potential energy curve obtained from the RKR1 program and vibrational wave functions for $v = 0$ to $v = 5$ (from bottom to top) obtained from the LEVEL program.

Table 4
Radiative Lifetimes (in ms) of ^{12}CH in the $X^2\Pi$ State

v'	1	2	3	4	5
Lifetime (τ)	7.98	4.20	2.98	2.40	2.09

The radiative lifetimes of CH have been calculated for vibrational levels $v = 1$, 2, 3, 4, and 5 of the $X^2\Pi$ state. The calculations include contributions from vibrational transitions with $\Delta v = 1$ and $\Delta v = 2$. As expected, the lifetimes decrease with an increase in the vibrational level. To our knowledge, no theoretical or experimental values of these lifetimes are currently available for comparison.

We provide the log file and PDM function calculated in this work as supplementary material in MRT format. The line list, along with the new ACE-FTS solar absorption spectrum, is available on Zenodo and can be accessed via the doi:10.5281/zenodo.19916162. The logfile includes the lines from R. Colin & P. F. Bernath (2010) and our newly assigned lines for the 4–3 and 5–4 vibrational bands of the $X^2\Pi$–$X^2\Pi$ state of CH. The logfile contains the rotational quantum number of upper (J') and lower (J'') states, parity of upper (P') and lower (P'') states, observed line positions (Obs.), calculated line positions (Calc.), difference between observed and calculated line positions (Obs.–Calc.), and line assignments. Similarly, the line list includes rotational quantum number of upper (J') and lower (J'') states, parity

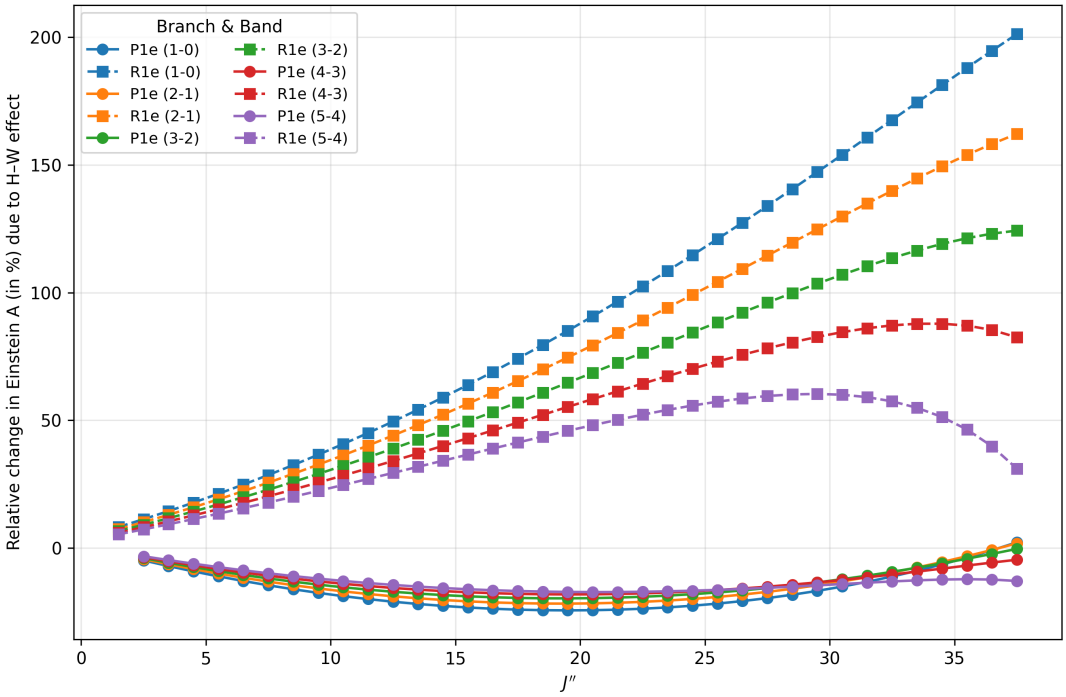

Figure 4. Comparison of Einstein A before and after employing the H-W effect. The x-axis shows the rotational quantum number (J''), while the y-axis indicates the percentage difference between the Einstein A values before and after applying the H-W effect.

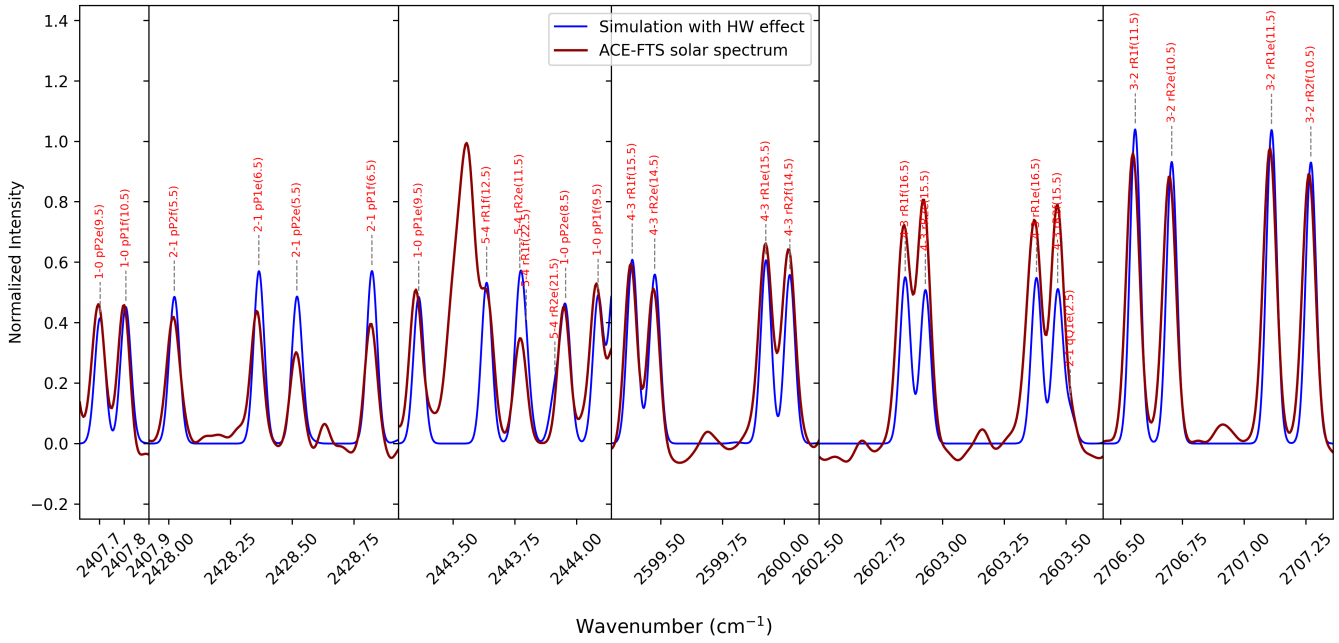

Figure 5. A comparison of line intensities between the simulation and the solar spectrum. The blue spectrum shows the simulation with the H-W effect, and the dark red spectrum shows the solar spectrum.

of upper (P') and lower (P'') states, line positions, Intensity, estimated uncertainty (Est. Unc.), energy levels for both upper (E_{up}) and lower (E_{low}) states, Einstein A coefficients, oscillator strengths (f), and line assignments. The line list contains the lines for the 1–0, 2–1, 3–2, 4–3, and 5–4 vibrational bands of ^{12}CH for J values up to 39.5.

5. Conclusion

The $X^2\Pi$ state of the CH radical has been reanalyzed, and the spectroscopic constants for the levels $v = 4$ and $v = 5$ of the $X^2\Pi$ state have been updated. A new dipole moment function for the $X^2\Pi$ state has been calculated and compared with existing values in the literature. The dipole moment,

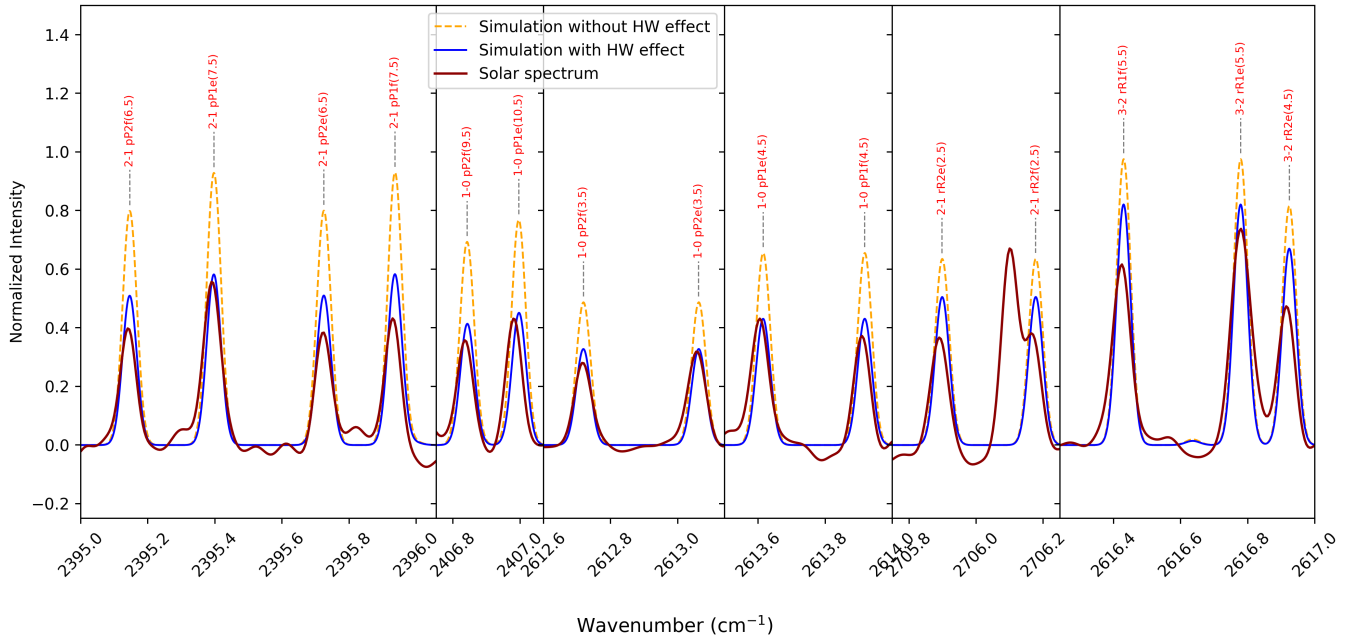

Figure 6. A comparison of the line intensities for simulated lines with and without the H-W effect with the ACE-FTS solar spectrum. The blue curve represents the simulated spectrum with the H-W effect, the dashed orange curve represents the simulated spectrum without the H-W effect, and the dark red curve shows the ACE-FTS solar absorption spectrum.

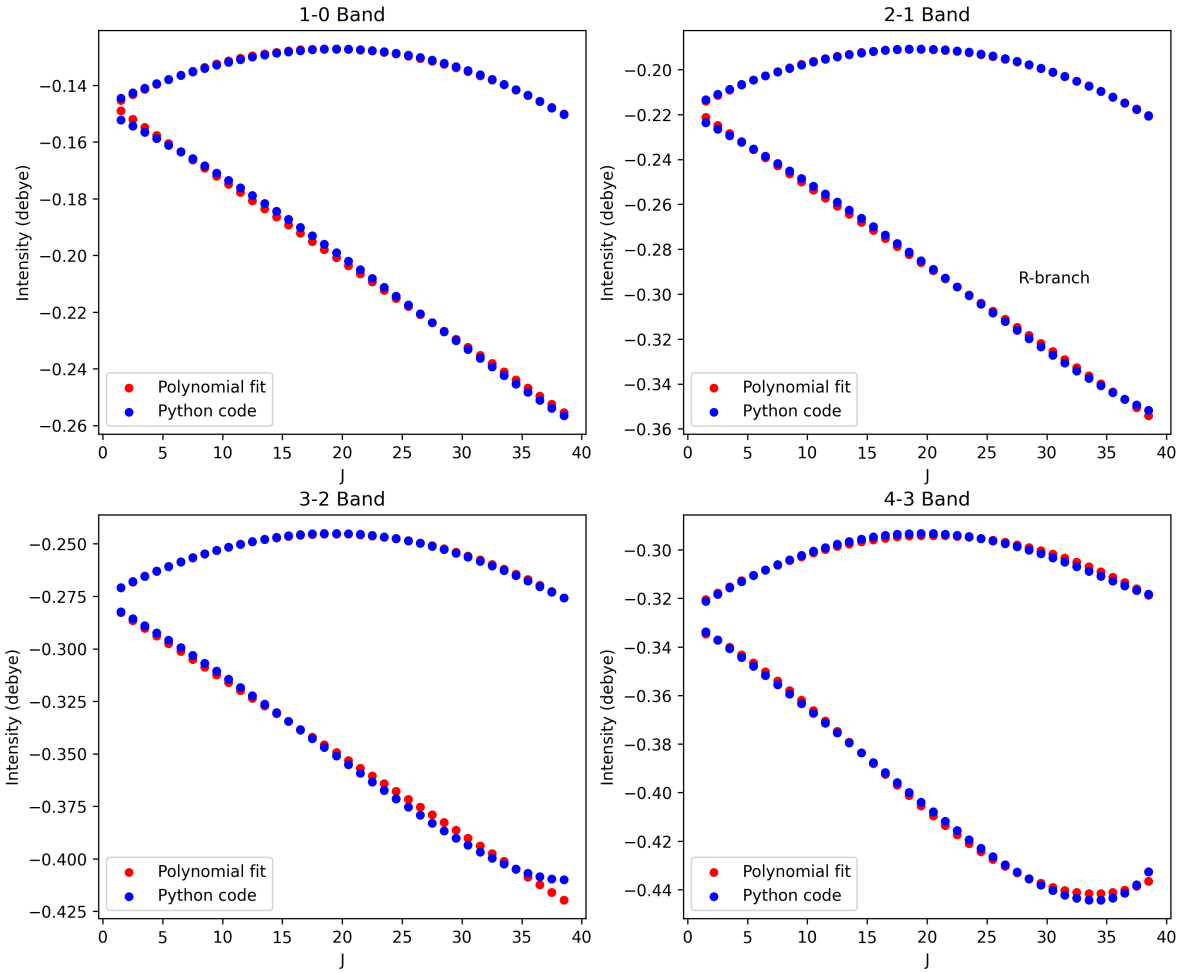

Figure 7. A comparison of two approaches to convert N dependent to J dependent intensities. The blue dots represent the method of polynomial fit as used by T. Masseron et al. (2014), and the red dots represent the method employed in this work.

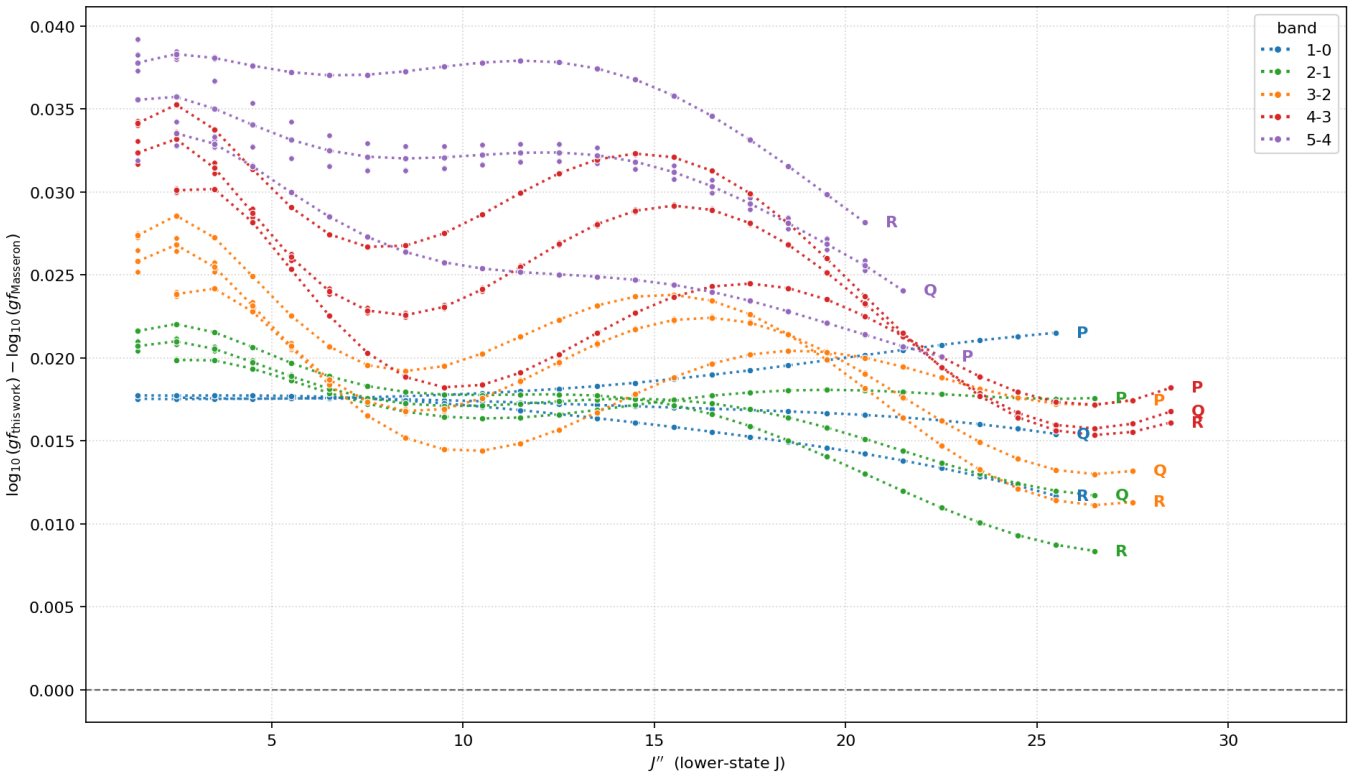

Figure 8. A comparison of gf values from from this work and T. Masseron et al. (2014). The difference between $\log_{10}(gf)$ values calculated in this work and T. Masseron et al. (2014) is plotted as a function of the rotational quantum number of the lower state. The dashed lines connect points for the P, Q, and R branches corresponding to the vibrational levels.

along with the G_v and B_v coefficients, was used in RKR and LEVEL programs to calculate the line strengths. The H-W effect was considered in the calculation to account for the rotational dependence of line intensities. This correction resulted in a reduction of the intensities for the P-branch transitions, while enhancing the intensities for the R-branch transitions as the rotational quantum number increased. The new line intensities align more closely with the ACE-FTS solar spectrum. For the first time, the radiative lifetime of CH in different vibrational levels of the $X^2\Pi$ state has been reported. Finally, an updated line list with line strengths has been provided, which is expected to be useful for determining the abundance of CH in various astrophysical environments.

Acknowledgments

The ACE mission is funded by the Canadian Space Agency (9F045-230412/001). Financial support was also provided by the NASA Laboratory Astrophysics Program (80NSSC24K1750). P.B. acknowledges R. F. B. for productive discussion.

ORCID iDs

Manish Bhusal https://orcid.org/0009-0008-6042-3271
Peter F. Bernath https://orcid.org/0000-0002-1255-396X
Léo Lavy https://orcid.org/0000-0003-4572-8612
Chris D. Boone https://orcid.org/0000-0001-9041-8299

References

Abrams, M., Goldman, A., Gunson, M., Rinsland, C., & Zander, R. 1996, ApOpt, 35, 2747
Bernath, P. 1987, JChPh, 86, 4838
Bernath, P., Brazier, C., Olsen, T., et al. 1991, JMoSp, 147, 16
Bernath, P. F. 2025, Spectra of Atoms and Molecules (5th ed.; Oxford Univ. Press)
Black, J., & Dalgarno, A. 1973, ApL, 15, 79
Brooke, J. S., Bernath, P. F., Western, C. M., et al. 2016, JQSRT, 168, 142
CDMS 2026, Molecules in Space, https://cdms.astro.uni-koeln.de/classic/molecules
Colin, R., & Bernath, P. F. 2010, JMoSp, 263, 120
Cui, J., Xu, J.-G., Qi, J.-X., Dou, G., & Zhang, Y.-G. 2018, ChPhB, 27, 103101
Danks, A., Federman, S., & Lambert, D. 1984, A&A, 130, 62
Dunning, T. H., Jr. 1989, JChPh, 90, 1007
Engeln, R., Letourneur, K., Boogaarts, M., Van de Sanden, M., & Schram, D. 1999, CPL, 310, 405
Furtenbacher, T., Hegedus, S. T., Tennyson, J., & Császár, A. G. 2022, PCCP, 24, 19287
Ghosh, P., Deo, M., & Kawaguchi, K. 1999, ApJ, 525, 539
Hase, F., Wallace, L., McLeod, S. D., Harrison, J. J., & Bernath, P. F. 2010, JQSRT, 111, 521
Herman, R., & Wallis, R. F. 1955, JChPh, 23, 637
Heurlinger, T. 1918, Untersuchungen über die Struktur der Bandenspektra, PhD thesis, Lunds universitet
Hou, Z., & Liu, L. 2024, PCCP, 27, 367
Jackson, M., Zink, L. R., McCarthy, M. C., Perez, L., & Brown, J. M. 2008, JMoSp, 247, 128
Jacob, A. M., Menten, K. M., Wiesemeyer, H., et al. 2020, A&A, 640, A125
Kepa, R., Para, A., Rytel, M., & Zachwieja, M. 1996, JMoSp, 178, 189
Kreplin, D. A., Knowles, P. J., & Werner, H.-J. 2019, JChPh, 150, 194106
Le Roy, R. J. 2017a, JQSRT, 186, 158
Le Roy, R. J. 2017b, JQSRT, 186, 167
Li, X., Kumar, A., Hsiao, C.-C., & Lee, Y.-P. 1999, JPCA, 103, 6162
Lie, G. C., Hinze, J., & Liu, B. 1973a, JChPh, 59, 1872
Lie, G. C., Hinze, J., & Liu, B. 1973b, JChPh, 59, 1887
Masseron, T., Plez, B., Van Eck, S., et al. 2014, A&A, 571, A47
McCarthy, M., Mohamed, S., Brown, J., & Thaddeus, P. 2006, PNAS, 103, 12263
McKellar, A. 1940, PASP, 52, 312
Medcraft, C., Linnartz, H., & Ubachs, W. 2019, JMoSp, 360, 15

Mélen, F., Grevesse, N., Sauval, A., et al. 1989, JMoSp, 134, 305
Nicolet, M. 1938, ZA, 15, 154
Phelps, D. H., & Dalby, F. W. 1966, PhRvL, 16, 3
Pritchard, B. P., Altarawy, D., Didier, B., Gibson, T. D., & Windus, T. L. 2019, J. Chem. Inf. Model., 59, 4814
Rangwala, N., Maloney, P. R., Glenn, J., et al. 2014, ApJ, 788, 147
Rydbeck, O., Elldér, J., & Irvine, W. 1973, Natur, 246, 466
Schroetter, I., Berné, O., Goicoechea, J., et al. 2025, A&A, 699, L13
Werner, H., Knowles, P. J., Knizia, G., Manby, F. R., & Schütz, M. 2011, WIREs Comp. Mol. Sci., 2, 242
Werner, H.-J., & Knowles, P. J. 1985, JChPh, 82, 5053
Werner, H.-J., & Knowles, P. J. 1988, JChPh, 89, 5803
Werner, H.-J., Knowles, P. J., & Knizia, G. 2022, MOLPRO, v2012.1, https://www.molpro.net
Werner, H.-J., Knowles, P. J., Manby, F. R., et al. 2020, JChPh, 152, 144107
Western, C. M. 2017, JQSRT, 186, 221
Whiteoak, J., Gardner, F., & Höglund, B. 1980, MNRAS, 190, 17P
Wiesemeyer, H., Güsten, R., Menten, K. M., et al. 2018, A&A, 612, A37
Woon, D. E., & Dunning, T. H., Jr. 1994, JChPh, 100, 2975
Zachwieja, M. 1995, JMoSp, 170, 285